Wireless Power Transfer

ARTICLE

Open Access

https://doi.org/10.48130/wpt-0025-0032

Wireless Power Transfer **2025**, 12: e033

Frequency-time domain combined analysis method for bidirectional wireless power transfer system based on single-stage AC-AC converter

Xi Zhang[1,2], Qianfan Zhang[1,2*], Hongxing Wu[3] and Shuai Dong[1,2]

[1] *Harbin Institute of Technology, Harbin 150080, China*
[2] *Harbin Institute of Technology Zhengzhou Research Institute, Zhengzhou 450046, China*
[3] *Fuyao University of Science and Technology, Fuzhou 350000, China*
* Corresponding author, E-mail: zhang_qianfan@hit.edu.cn

Abstract

The First-Harmonic Approximation (FHA) analysis method is widely utilized in Bidirectional Wireless Power Transfer (BWPT) systems, providing simplified input and output characteristics. However, in complex systems and varying operating conditions, such as those involving a single-stage AC-AC converter, the FHA method falls short, leading to significant calculation deviations that fail to accurately represent the system's working state, as the same as Traditional Multi-harmonics methods (TMH), and time-domain only derivation methods. This paper introduces a novel Frequency-Time Domain Combined (FTDC) analysis prediction method that enhances the precision of the system's operational analysis through theoretical calculations. The proposed method integrates frequency domain analysis with time domain analysis to reconstruct the system's voltage and current waveforms via data deduction and iteration. Notably, this approach outperforms simulation software by rapidly yielding the steady-state waveform and directly providing essential data, including Root Mean Square (RMS) values, amplitude values, and zero-crossing points. This efficiency aids in the expedited and improved design of the entire BWPT system. Finally, the accuracy and practicality of the proposed method are validated through a combination of theoretical analysis and experimental results.

Citation: Zhang X, Zhang Q, Wu H, Dong S. 2025. Frequency-time domain combined analysis method for bidirectional wireless power transfer system based on single-stage AC-AC converter. *Wireless Power Transfer* 12: e033 https://doi.org/10.48130/wpt-0025-0032

Introduction

Bidirectional Wireless Power Transfer (BWPT) systems are essential in the context of electric vehicles (EVs), enabling the efficient bidirectional power exchange between the Grid and Vehicle (G2V), and Vehicle to Grid (V2G) operations[1–4].

In BWPT systems, the traditional two-stage converter structure at the transmitter suffers from drawbacks such as large volume, high cost, and complex control[1]. Consequently, replacing the conventional two-stage structure with a single-stage AC-AC converter at the transmitter has become a current research trend in BWPT systems. Among single-stage AC-AC converters, the matrix converter eliminates the large-capacitance DC bus capacitor but still requires eight high-frequency switches[5–8]. Moreover, it faces issues such as low voltage gain, significant dead-time effects, and limited soft-switching capability. The buck–boost type single-stage AC-AC converter reduces the number of switches compared to the matrix converter[9–12], but it does not resolve the soft-switching limitations. The Bridgeless Full Bridge (BFB) converter halves the number of switches and offers advantages such as high voltage gain and a wide soft-switching range[13]; however, it retains large electrolytic capacitors, and its control system is still highly complex.

In contrast, the single-stage totem-pole converter strikes a compromise, eliminating the drawbacks of the above topologies while combining the benefits of fewer switches, a small DC bus capacitor, and high voltage gain[14]. Furthermore, with Triple Phase Ratio Shift (TPRS) control, it not only achieves power factor correction (PFC) but also further expands the soft-switching range of the system[15]. Nevertheless, current research on BWPT systems employing totem-pole converters, as presented in this paper, remains limited; the modeling and analysis of such systems is critical for optimizing their performance and ensuring reliable power transmission.

A range of approaches has been proposed for the circuit analysis of BWPT systems, each serving specific purposes. In passive network analysis, a spatial state model is introduced that represents the parameters of passive networks[16], along with voltage and current, in matrix form. This representation simplifies the calculation process, albeit at the expense of model realism and detail. Another study[17] proposed a steady-state model for BWPT systems, focusing on the effects of battery voltage fluctuations in EVs under varying load conditions. Both these methods rely on the FHA, which simplifies the voltage transformation in the converter by considering only the effective value in the fundamental state, thereby neglecting the time-domain dynamics of the system.

Beyond the FHA method, researchers have explored alternative ways to analyze BWPT systems. Notably, the harmonics current method[18,19] that decomposes the current in passive networks, treating each harmonic component as an independent passive network. This approach, while offering reasonable accuracy, requires additional components such as filters, which can increase the system's size and losses. The multi-harmonics analysis method[20] offers a more comprehensive approach by decomposing complex voltage and current waveforms into their harmonic components in the frequency domain. It analyzes higher-order harmonics and reconstructs the waveforms to approximate the actual voltage and current values. However, this method has a significant drawback: its inability to integrate with the time domain limits its effectiveness, particularly in capturing the phase differences between the primary and secondary voltages in bidirectional systems.

These methods are collectively referred to as Traditional Multi-harmonics (TMH) techniques, which, while accurate in the frequency domain, lack phase correction in time-domain processing. This is particularly problematic in BWPT systems based on single-stage AC-AC converters, where both the amplitude and phase of voltage

and current in the passive network continuously fluctuate due to grid voltage variations. As a result, accurately modeling these systems under such complex operating conditions remains a significant challenge when using TMH methods.

To address the limitations of TMH methods, several researchers have suggested time-domain-based approaches. The sampled-data modeling method[21] is proposed for analyzing the system parameters of BWPT, ensuring accuracy through time-domain calculations. However, this method is limited to sinusoidal current analysis and does not apply to non-sinusoidal currents in Double LCC (DLCC) systems. Other studies[22,23] introduced discrete time-domain models that decompose and synthesize current solutions over different time intervals to reconstruct waveforms. However, these models are restricted to networks with a single voltage source. When additional complexities, such as active rectifiers on the secondary side and phase shifts between the primary and secondary sides, are introduced, the models become significantly more complicated. This often results in complex mathematical derivations that are difficult to apply under dynamic BWPT operating conditions. Furthermore, despite considering all possible scenarios, these approaches struggle to provide convergent solutions, leading many researchers to rely more on simulation tools than theoretical models.

In this context, this paper proposes a novel Frequency-Time Domain Combined (FTDC) analysis prediction method for BWPT systems[24]. This method employs a single-stage totem-pole AC-AC converter to integrate both time-domain and frequency-domain analyses. The approach provides accurate square wave voltages, precise sine currents, and relatively accurate non-sinusoidal currents in passive networks. By extracting key parameters such as amplitude, phase, effective value, and zero-crossing points, this method enables more accurate predictions of actual system behavior.

The paper proceeds by first establishing the theoretical framework for the BWPT high-order harmonics model. It then derives the system characteristic variables using the combined frequency and time-domain methods, producing theoretical predictions. To validate these findings, an experimental platform is developed, and the collected data is analyzed to assess the accuracy and practical applicability of the proposed FTDC method.

This paper begins by establishing and deriving the BWPT high-order harmonics model through theoretical analysis. It then derives the system characteristic variables using a combination of frequency and time-domain methods, resulting in theoretical predictions. An experimental platform was subsequently set up to validate the accuracy of these theoretical findings. Finally, the collected data were organized and analyzed to evaluate both the accuracy and practical applicability of the proposed FTDC analysis method.

Concept of the proposed analysis method

Figure 1a illustrates the schematic circuit of the BWPT system, which is based on a single-stage AC-AC converter utilized in this paper. The primary converter is designed with a single-stage totem pole structure, while the secondary converter employs an active rectifier. The compensation network is configured using a DLCC structure. Figure 1b presents the equivalent circuit, and the expressions for each passive impedance are detailed in Table 1.

Figure 2a depicts the schematic diagram of the AC side voltage at the primary and secondary sides. This paper adopts a three-shift-ratio control mode, wherein the target control parameters are achieved by adjusting the internal phase shift of the primary side totem-pole converter (or called totem converter), the internal phase shift ratio of the secondary side active bridge, and the external shift ratio comparison between the primary and secondary side converters.

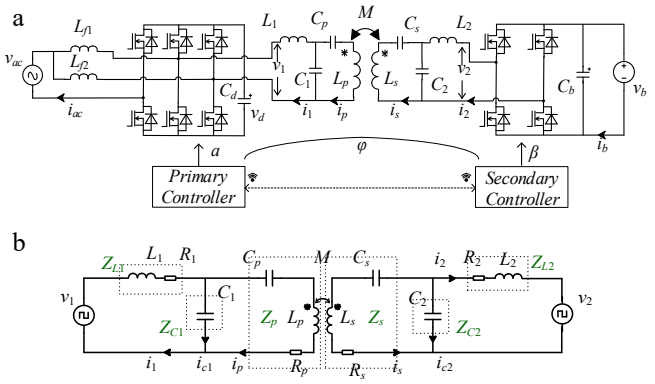

Fig. 1 Schematic of BWPT system. (a) BWPT circuit with totem converter. (b) Equivalent circuit with linear elements.

Table 1. Expression of impedance in passive network.

Symbol	Concept	Expression
Z_{L1}	Transmitter side filter inductor impedance	$R_1 + j\omega ML_1$
Z_{C1}	Transmitter side filter capacitor impedance	$1/j\omega C_1$
Z_p	Transmitter side series impedance	$R_p + j\omega L_p + 1/j\omega C_p$
Z_s	Receiver side series impedance	$R_s + j\omega L_s + 1/j\omega C_s$
Z_{L2}	Receiver side filter inductor impedance	$R_2 + j\omega ML_2$
Z_{C2}	Receiver side filter capacitor impedance	$1/j\omega C_2$

Figure 2b, c explains why a time-domain only analysis method can't derive an accurate model for the single-stage BWPT system possessing phase shift delay. When β changes from medium to small, the voltage sequence between the primary side and the secondary side changes, resulting in the established model being completely rebuilt from scratch. Not to mention, the time-varying nature of the phase shift will also lead to inaccuracies in the frequency-domain TMH method due to the constantly changing phase difference.

In conclusion, they fail to capture various critical details during transient conditions. This includes the amplitudes of voltage and current, the soft switching states of the converter, and other dynamic behaviors.

To address these limitations and enable rapid predictions of the system's working state without reliance on simulation or experimental platforms, this paper proposes an FTDC method that balances between the frequency domain and time domain analysis.

First, the harmonics frequency AC side voltages v_1 and v_2 of the primary and secondary side can be expressed as:

$$v_{1,n}(t) \underset{n=1,3,5\cdots}{=} \frac{4}{\pi} V_d \frac{1}{n} \cos\left(n\omega t - \frac{n\alpha}{2}\right) \sin\left(\frac{n\alpha}{2}\right) \tag{1}$$

$$v_{2,n}(t) \underset{n=1,3,5\cdots}{=} \frac{4}{\pi} V_b \frac{1}{n} \cos\left(n\omega t - \frac{n\alpha}{2} + n\varphi\right) \sin\left(\frac{\beta}{2}\pi\right) \tag{2}$$

where, α, β, and φ are three shift ratios of the primary and secondary side voltages. V_d and V_b are the steady values of the DC bus voltage of the primary and secondary converter of v_d and v_b, respectively. n is the order of harmonics. ω is the working frequency of the system, and the system generally works at the resonant frequency ω_c.

$$\omega_c = \frac{1}{\sqrt{L_1 C_1}} = \frac{1}{\sqrt{L_2 C_2}} \tag{3}$$

$$\omega_c = \frac{1}{\sqrt{\frac{L_p\left(C_1 + C_p\right)}{C_1 C_p}}} = \frac{1}{\sqrt{\frac{L_s\left(C_2 + C_s\right)}{C_2 C_s}}} \tag{4}$$

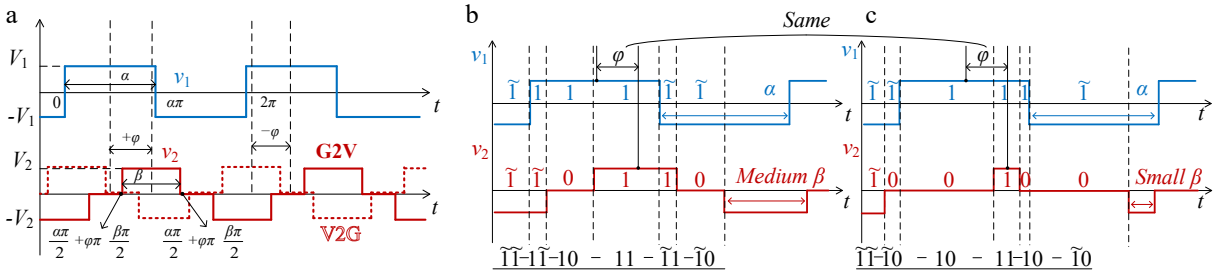

Fig. 2 Schematic of transmitter and receiver side voltage phase shift. (a) Bidirectional voltage phase delay schematic. (b) Medium β for the system. (c) Small β for the system.

FTDC analysis aims to theoretically represent the voltage and current waveforms of passive networks. According to Eqs (1) and (2), when employing the FHA method, only the fundamental voltage component is typically selected as the primary factor for calculations. However, it is essential to consider the higher-order harmonics of the voltage and current. The independent variable matrix $\boldsymbol{x}$ of the passive network can be expressed as:

$$\boldsymbol{x}=\begin{bmatrix} v_{1,1} & i_{1,1} & i_{p,1} & i_{s,1} & i_{2,1} & v_{2,1} \\ v_{1,3} & i_{1,3} & i_{p,3} & i_{s,3} & i_{2,3} & v_{2,3} \\ \vdots & \vdots & \vdots & \vdots & \vdots & \vdots \\ v_{1,n} & i_{1,n} & i_{p,n} & i_{s,n} & i_{2,n} & v_{2,n} \end{bmatrix}^{T} \tag{5}$$

According to the KCL and KVL equations, the n_{th} harmonics coefficient matrix $\boldsymbol{A}_n$ can be expressed as:

$$\boldsymbol{A}_n=\begin{bmatrix} 1 & -(Z_{L1,n}+Z_{C1,n}) & Z_{C1,n} & 0 & 0 & 0 \\ 1 & -Z_{L1,n} & -Z_{p,n} & jn\omega M & 0 & 0 \\ 0 & 0 & jn\omega M & -Z_{s,n} & -Z_{L2,n} & -1 \\ 0 & 0 & 0 & Z_{C2,n} & -(Z_{L2,n}+Z_{C2,n}) & -1 \end{bmatrix} \tag{6}$$

$$\boldsymbol{A}=diag\{\boldsymbol{A}_1,\boldsymbol{A}_3,\boldsymbol{A}_5,\cdots\boldsymbol{A}_n\} \tag{7}$$

$$\boldsymbol{A}\boldsymbol{x}=\boldsymbol{O}_{4n\times n} \tag{8}$$

If the square wave voltage is decomposed into its constituent sinusoidal high-order harmonics currents using the homogeneous theorem, the aforementioned frequency domain calculation method can be effectively applied during each complete cycle of operation. This approach allows for a more accurate representation of the system's behavior by considering the contributions of each harmonics component to the overall waveform, facilitating better analysis and design of passive networks.

Based on the homogeneous theorem, the voltage and current within the passive network can be decomposed into various harmonic components. With a specific number of harmonics considered, the passive impedance network will exhibit relevant characteristics at those corresponding frequencies. Each individual circuit can be analyzed in the frequency domain to satisfy the relationships defined by the state equations. This approach allows for the derivation of a new state equation that reflects the behavior of the network under the influence of these harmonics. Figure 3 is a schematic diagram of the phase of voltage and current in a passive network within a BWPT system. Taking G2V as an example, v_1 leading i_1 ensures one of the basic conditions for ZVS of the primary side converter. Regardless of how the phase shift φ changes, i_p and v_1, as well as i_s and v_2, always maintain an almost $\pi/2$ phase difference.

Further derivation of Eq. (2) using the Trigonometric function[25]

$$v_{2,n}(t)=\frac{4}{\pi}V_b\frac{1}{n}\begin{pmatrix}\cos\left(n\omega t-\frac{n\alpha}{2}\right)\cos(n\varphi)\\ -j\cos\left(n\omega t-\frac{n\alpha}{2}\right)\sin(n\varphi)\end{pmatrix}\sin\left(\frac{n\beta}{2}\right) \tag{9}$$

We can get

$$v_{2,n}(t)=\frac{4}{\pi}(\cos(\varphi)+j\sin(\varphi))\cos\left(n\omega_s t-\frac{\alpha\pi}{2}\right)\sin\left(\frac{\beta\pi}{2}\right)V_b \tag{10}$$

Through derivation, the secondary side current i_2 can be expressed as:

$$i_{2,n}=\frac{Z_{C1,n}}{\Psi_{2,n}}v_{1,n}+\frac{\Psi_{1,n}}{\Psi_{2,n}}v_{2,n} \tag{11}$$

where,

$$\begin{aligned}\Psi_{1,n}=&\frac{jn\omega M}{Z_{C2,n}}(Z_{L1,n}+Z_{C1,n})-\\&\frac{1}{jn\omega M}\left(Z_{p,n}(Z_{L1,n}+Z_{C1,n})+Z_{C1,n}Z_{L1,n}\right)\left(\frac{Z_{s,n}}{Z_{C2,n}}+1\right)\end{aligned} \tag{12}$$

$$\begin{aligned}\Psi_{2(n)}=&\frac{1}{jn\omega M}\left(Z_{p,n}(Z_{L1,n}+Z_{C1,n})+Z_{C1,n}Z_{L1,n}\right)\left(\frac{Z_{L2,n}}{Z_{C2,n}}Z_{s,n}\right.\\&\left.+Z_{s,n}+Z_{L2,n}\right)\\&-jn\omega M\left(\frac{Z_{L2,n}}{Z_{C2,n}}+1\right)(Z_{L1,n}+Z_{C1,n})\end{aligned} \tag{13}$$

$$\boldsymbol{\Psi}_1=diag\{\Psi_{1,1},\Psi_{1,3},\Psi_{1,5},\cdots\Psi_{1,n}\} \tag{14}$$

$$\boldsymbol{\Psi}_2=diag\{\Psi_{2,1},\Psi_{2,3},\Psi_{2,5},\cdots\Psi_{2,n}\} \tag{15}$$

The time-domain representation of matrix $\boldsymbol{i}_2$, which includes multiple harmonics, is as follows:

$$\boldsymbol{i}_2(t)=\boldsymbol{x}_{:,5}(t)=(\boldsymbol{Z}_{C1}\boldsymbol{v}_1(t)+\boldsymbol{\Psi}_1\boldsymbol{v}_2(t))\boldsymbol{\Psi}_2^{-1} \tag{16}$$

$$\boldsymbol{i}_2(t)=\boldsymbol{x}_{:,5}(t)=\boldsymbol{Y}_{21}\boldsymbol{v}_1(t)+\boldsymbol{Y}_{22}\boldsymbol{v}_2(t) \tag{17}$$

where, $\boldsymbol{Y}_{21}$ and $\boldsymbol{Y}_{22}$ are the coefficient admittance matrix, corresponding to v_1 and v_2 respectively. Based on $i_{2(n)}$, other current expressions i_p, i_1, i_s in passive networks can be derived

$$i_{p,n}=\frac{1}{jn\omega M}\left(\frac{i_{2,n}Z_{L2,n}+v_{2,n}}{Z_{C2,n}}Z_{s,n}+i_{2,n}(Z_{s,n}+Z_{L2,n})+v_{2,n}\right) \tag{18}$$

$$\boldsymbol{i}_p=\begin{bmatrix} i_{p,1} & i_{p,3} & \cdots & i_{p,n} \end{bmatrix} \tag{19}$$

$$\boldsymbol{i}_p(t)=\boldsymbol{x}_{:,3}(t)=\boldsymbol{Y}_{p1}\boldsymbol{v}_1(t)+\boldsymbol{Y}_{p2}\boldsymbol{v}_2(t) \tag{20}$$

$$i_{1,n}=\frac{v_{1,n}+i_{p,n}Z_{C1,n}}{Z_{L1,n}+Z_{C1,n}} \tag{21}$$

$$\boldsymbol{i}_1=\begin{bmatrix} i_{1,1} & i_{1,3} & \cdots & i_{1,n} \end{bmatrix} \tag{22}$$

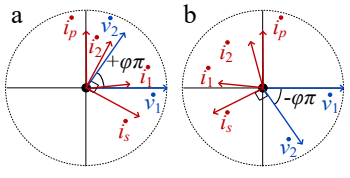

Fig. 3 Schematic diagram of voltage and current phases in a passive network. (a) G2V. (b) V2G.

$$\boldsymbol{i}_1(t) = \boldsymbol{x}_{:,1}(t) = \boldsymbol{Y}_{11}\boldsymbol{v}_1(t) + \boldsymbol{Y}_{12}\boldsymbol{v}_2(t) \tag{23}$$

$$i_{s,n} = \frac{i_{2,n}Z_{L2,n} + v_{2,n}}{Z_{C2,n}} + i_{2,n} \tag{24}$$

$$\boldsymbol{i}_s = \begin{bmatrix} i_{s,1} & i_{s,3} & \cdots & i_{s,n} \end{bmatrix} \tag{25}$$

$$\boldsymbol{i}_s(t) = \boldsymbol{x}_{:,4}(t) = \boldsymbol{Y}_{s1}\boldsymbol{v}_1(t) + \boldsymbol{Y}_{s2}\boldsymbol{v}_2(t) \tag{26}$$

where, $\boldsymbol{Y}_{p1}$ and $\boldsymbol{Y}_{p2}$, $\boldsymbol{Y}_{11}$ and $\boldsymbol{Y}_{12}$, $\boldsymbol{Y}_{s1}$ and $\boldsymbol{Y}_{s2}$, are the coefficient matrix corresponding to each current. The parameters of the BWPT system presented in this paper are detailed in Table 2. Figure 4a–d shows the amplitude-phase characteristic diagrams of the coefficient admittance matrix. At the fundamental frequency, which corresponds to the resonant frequency, i_2 and i_s are independent of v_1 and exhibit a high correlation with v_2. Similarly, i_1 and i_p are independent of v_1 and show a high correlation with v_2. As the frequency increases to the 3_{rd}, 5_{th}, and higher harmonics, the amplitude attenuates, while the phase remains constant and exhibits a canceling effect.

Figure 5 shows the FFT analysis of the currents in the passive network. It can be observed that the component of the receiving current i_2 is less than 6% after the 3rd harmonic, thus higher-order harmonics can be ignored. Similarly, for the transmitting current i_1, the component after the 7th harmonic is also below 5%, making further harmonics negligible. Based on this, the harmonic order for superposition is set to 7.

$$\hat{i}_{1\_\varpi}(t) = \sum_{j=1}^{n} i_{1,j}(t),\ \hat{i}_{p\_\varpi}(t) = \sum_{j=1}^{n} i_{p,j}(t),\ n \in \mathbb{Z}^+ \tag{27}$$

$$\hat{i}_{s\_\varpi}(t) = \sum_{j=1}^{n} i_{s,j}(t),\ \hat{i}_{2\_\varpi}(t) = \sum_{j=1}^{n} i_{2,j}(t),\ n \in \mathbb{Z}^+ \tag{28}$$

The summation of the previous harmonics components is merely an expression in the frequency domain; the time domain and phase shift components need to be added. Voltage phase correction ratio φ_{v1_nth}、φ_{v2_nth} can be expressed as:

$$\varphi_{v1\_nth} = \frac{(n-1)\alpha\pi}{2},\ \varphi_{v2\_nth} = (n-1)\pi\left(\frac{\alpha}{2} + \varphi\right) \tag{29}$$

where, n equals to 1, 3, 5, 7, ···, based on the phase difference relationship between the voltages, the time-domain synthesis concept for the transmitting and receiving currents can be obtained through the previous frequency-domain superposition and subsequent phase correction, as shown in Fig. 6.

The passive network current synthesis can be expressed as:

$$\hat{i}_1(t) = \Im\left(\hat{i}_{1\_\varpi}\left(t - \frac{\varphi_{i1\_nth}}{\omega_c}\right)\right) \tag{30}$$

Table 2. Example parameters of BWPT system.

Symbol	Concept	Expression
L_1/R_1	Transmitter side filter inductor impedance / internal resistance	23 μH/0.02 Ω
C_1	Transmitter side filter capacitor impedance	152.43 nF
C_p	Transmitter side series capacitor	149.19 nF
L_p/R_p	Transmitter side series inductor / internal resistance	46.49 μH/0.02 Ω
L_2/R_2	Receiver side filter inductor impedance / internal resistance	14 μH/0.02 Ω
C_2	Receiver side filter capacitor impedance	250.42 nF
C_s	Receiver side series capacitor	246.55 nF
L_s/R_s	Receiver side series inductor / internal resistance	29.73 μH/0.02 Ω
f_c	Resonant frequency	85 kHz
f_l	Grid frequency	50 Hz
M	Mutual Inductor	10.04 μH

$$\hat{i}_2(t) = \Im\left(\hat{i}_{2\_\varpi}\left(t - \frac{\varphi_{i2\_nth}}{\omega_c}\right)\right) \tag{31}$$

$$\hat{i}_p(t) = \Im\left(\hat{i}_{p\_\varpi}\left(t - \frac{\pi}{2\omega_c}\right)\right), \hat{i}_s(t) = \Im\left(\hat{i}_{s\_\varpi}\left(t + \frac{\pi}{2\omega_c}\right)\right) \tag{32}$$

where, current phase correction ratios φ_{i1_nth}, φ_{i2_nth} can be expressed as:

$$\varphi_{i1\_nth} = (n-1)\pi\left(\frac{\alpha}{4} - abs(\tilde{\kappa}\varphi)\right) \tag{33}$$

$$\varphi_{i2\_nth} = (n-1)\pi\left(1 - \frac{\alpha}{4} + \beta - abs(\tilde{\kappa}\varphi)\right) \tag{34}$$

where, n equals to 1, 3, 5, 7, ···, k is the correction factor used to eliminate the phase impact caused by higher-order harmonics. The current waveforms derived by the FTDC model are shown in Fig. 3 compared with the practical experiment waveforms.

Control principles and theory analysis results

In the bidirectional wireless charging system discussed in this paper, it is essential to implement the Power Factor Correction (PFC) function on the network side. This can be achieved by adjusting the inward shift ratio β of the secondary converter. By doing so, the current on the network side can effectively align with the network side voltage, as illustrated in Fig. 7.

The grid side current i_{ac} can be obtained by the fundamental wave approximation method[6]

$$i_{ac} = \frac{16}{\pi^2} V_b \frac{M}{\omega_0 L_1 L_2} \sin\left(\frac{\alpha}{2}\pi\right) \sin\left(\frac{\beta}{2}\pi\right) \sin(\varphi\pi) \tag{35}$$

The control method in this paper is three-shift-ratio regulation control, in which α is 1 as the internal phase shift of the transmitter converter, to ensure that the transmitter converter works in a wide range of Zero Voltage Switching (ZVS). β realizes the PFC function of the system, φ is adjusted to realize the forward and reverse transmission of energy and power regulation.

Figure 8a–c shows the modeling comparison of the BWPT system when $\varphi = 0.5$. In Fig. 8a, the voltage and current under FHA are pure sine waves, which cannot be used in the field of accurate modeling; In Fig. 8b, although the TMH modeling has made breakthroughs in current amplitude and voltage shape, there are still problems of phase missing and peak gap. Under TMH, the model is always symmetrical about the center, which does not match the actual current waveform in Fig. 8d, and it is also impossible to accurately calculate the zero-crossing points and amplitude. In Fig. 8c, the FTDC method can ensure the consistency of the amplitude even when v_{ac} changes through phase correction, and can achieve good restoration from the perspective of amplitude and phase.per.

The theoretical voltage and current waveforms illustrated in Fig. 9 can be derived using the FTDC analysis method. In Fig. 9a–d, the left figures depict the transient voltage and current waveforms of the passive network when the network side voltage is at its maximum. Conversely, the right figures show the corresponding waveforms when the grid side voltage is low.

The coil currents i_p and i_s are sinusoidal, making it straightforward to extract their amplitude and phase information. Based on the theoretical data, key parameters such as the peak-to-peak value, effective value, and zero-crossing points of i_p and i_s can be easily calculated. While i_1 is equivalent to i_2, it is important to note that due to the unique characteristics of the LCC compensation network, i_1 and i_2 are non-sinusoidal. However, the waveform reconstructed using the FTDC method still closely resembles the expected shape. In addition to the amplitude, the zero-crossing points are clearly identifiable, and the effective value of the current can be computed using discrete integration.

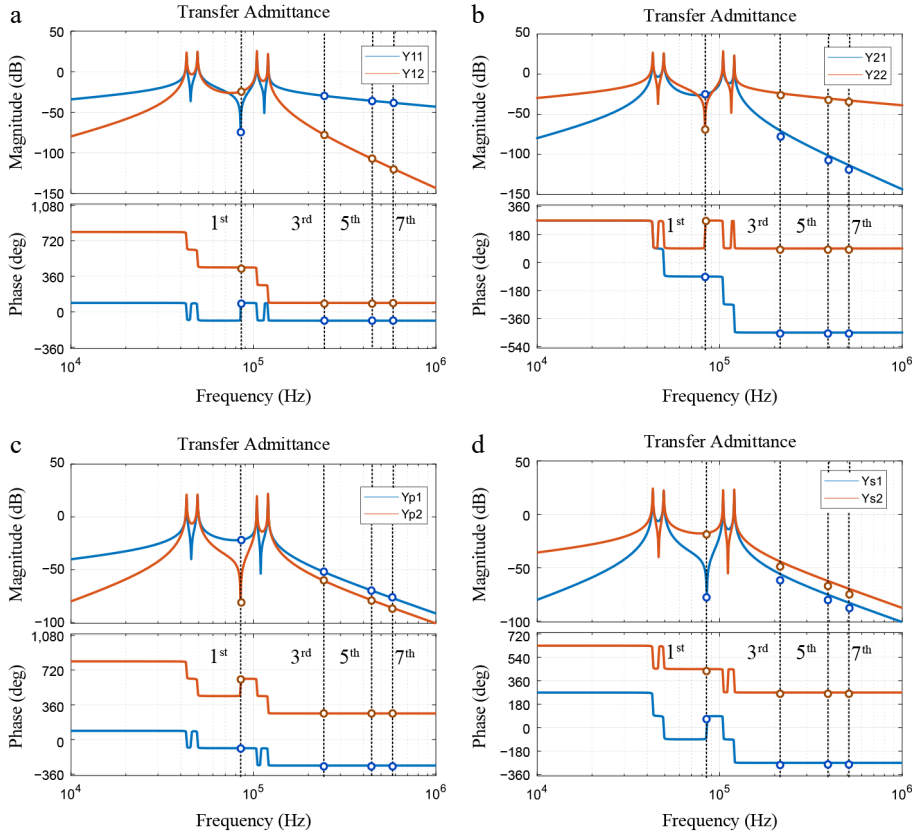

Fig. 4 Coefficient admittance matrix amplitude-phase characteristic diagram. (a) Y_{11} and Y_{12}. (b) Y_{21} and Y_{22}. (c) Y_{p1} and Y_{p2}. (d) Y_{s1} and Y_{s2}.

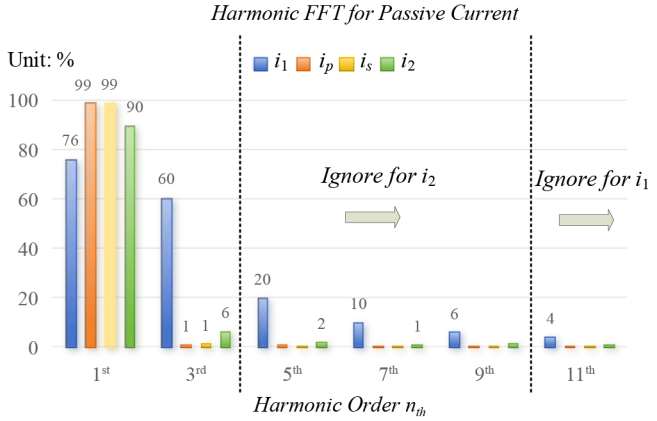

Fig. 5 Schematic diagram of the harmonics composition of each current.

$$\hat{X}_{pos\_RMS} = \sqrt{\frac{1}{T}\sum \hat{x}_{pos}^2(t)t_{step}} \tag{36}$$

$$\hat{X}_{pos\_Ap} = \max(abs(\hat{x}_{pos}(t))) \tag{37}$$

$$\hat{T}_{zero} = Solve(\hat{x}_{pos}(t) = 0) \tag{38}$$

where, x_{pos} represents i_1, i_2, i_p, and i_s. Root Mean Square (RMS) value X_{pos_RMS}, amplitude value X_{pos_Ap}, zero crossing point T_{zero} can be represented by Eqs (36)–(38). T is the period, and t_{step} is the time step. At the same time, according to the above data, the soft switching state of the converter can also be judged. For example, the relationship between v_1 and i_1 indicates that the primary side converter works in ZVS state.

Experiment validation

Figure 10 shows the BWPT system experiment test bench based on the single-stage totem pole AC-AC converter.

Figure 11a and b illustrate the voltage and current waveforms at the network side, as well as the voltage waveforms at the primary and secondary sides of the passive network. The primary side input voltage v_1 varies in response to the grid side voltage, while the amplitude of the secondary side voltage v_2 is influenced by the load voltage.

Figure 12 corresponds to Fig. 9a, Fig. 13 to Fig. 9b, Fig. 14 to Fig. 9c, and Fig. 15 to Fig. 9d. The dashed lines '---' in Figs 12–15 are depicted from the theoretical results in Fig. 9. The phase difference between the primary and secondary side voltages v_1 and v_2 is represented by a shift of φ. The left images correspond to the passive network waveforms when the grid voltage v_{ac} is at its maximum, while the right images represent the waveforms when the grid voltage v_{ac} is low.

The displayed waveforms demonstrate that the waveforms obtained through the FTDC theory (shown as dashed lines) closely align with those derived from actual experiments across a wide range of operating points. The primary input current i_1 exhibits a slight deviation in shape; this discrepancy arises from the interplay between the frequency and time domains, where the derivation of frequency domain impedance is the primary consideration. Consequently, it becomes challenging to accurately capture the waveform variations within a single cycle. Nonetheless, the final amplitude, effective value, and zero-crossing points show strong agreement with experimental results, thereby validating the effectiveness of the FTDC method.

The FTDC method integrates both time-domain and frequency-domain analysis techniques. Essentially, the final voltage and

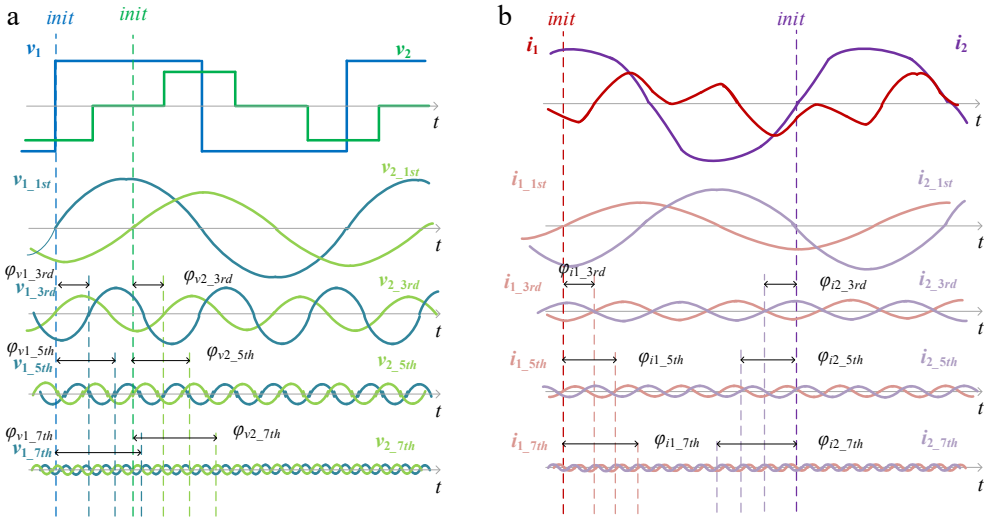

Fig. 6 Phase correction for passive network voltage and current. (a) Voltage v_1 and v_2. (b) Current i_1 and i_2.

current waveforms are derived by superimposing sinusoidal waves over the complete period of each harmonic. As a result, there may be slight discrepancies in shape when compared to experimental waveforms. However, in terms of amplitude, phase, effective value, and zero-crossing points, the FTDC method proves to be more suitable for experimental applications. However, under the TMH method, the calculation of the peak has a significant deviation, not to mention the FHA method. As the phase shift ratio φ decreases, the gap between the theoretical value and the actual value becomes larger.

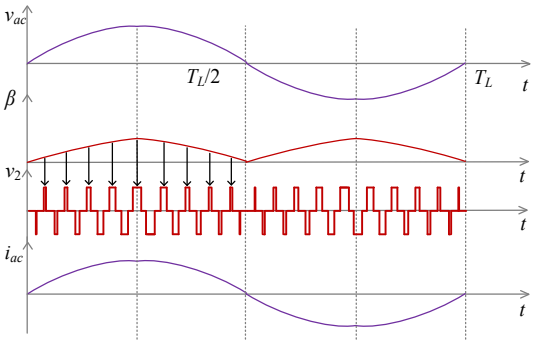

Fig. 7 Waveforms of PFC control using the β regulation method.

Figure 16 shows the comparison between theoretical and experimental current error data when the grid-side voltage v_{ac} reaches its maximum. The current error *err* is defined as:

$$err = \frac{i_{exp} - i_{thy}}{i_{pp\_exp}} \times 100\% \tag{39}$$

where, i_{exp} is experiment current, i_{thy} is theoretical calculation current, i_{pp_exp} is peak-peak experiment current.

The current errors of i_2, i_p, i_s are guaranteed to stay within 5%, reflecting the accuracy of the FTDC analysis method. However, the

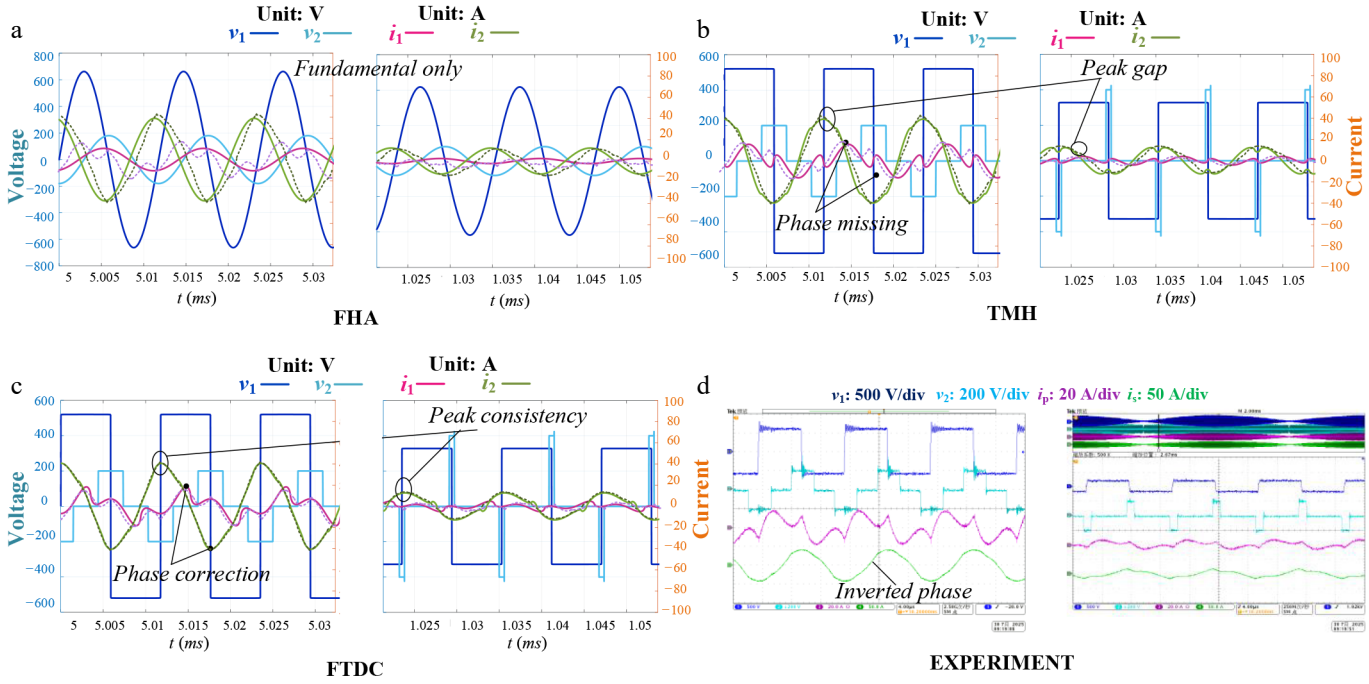

Fig. 8 Theory derivation comparison under φ = 0.5 for G2V (left: max grid voltage v_{ac}; right: low grid voltage v_{ac}). (a) FHA. (b) TMH. (c) FTDC. (d) Experiment.

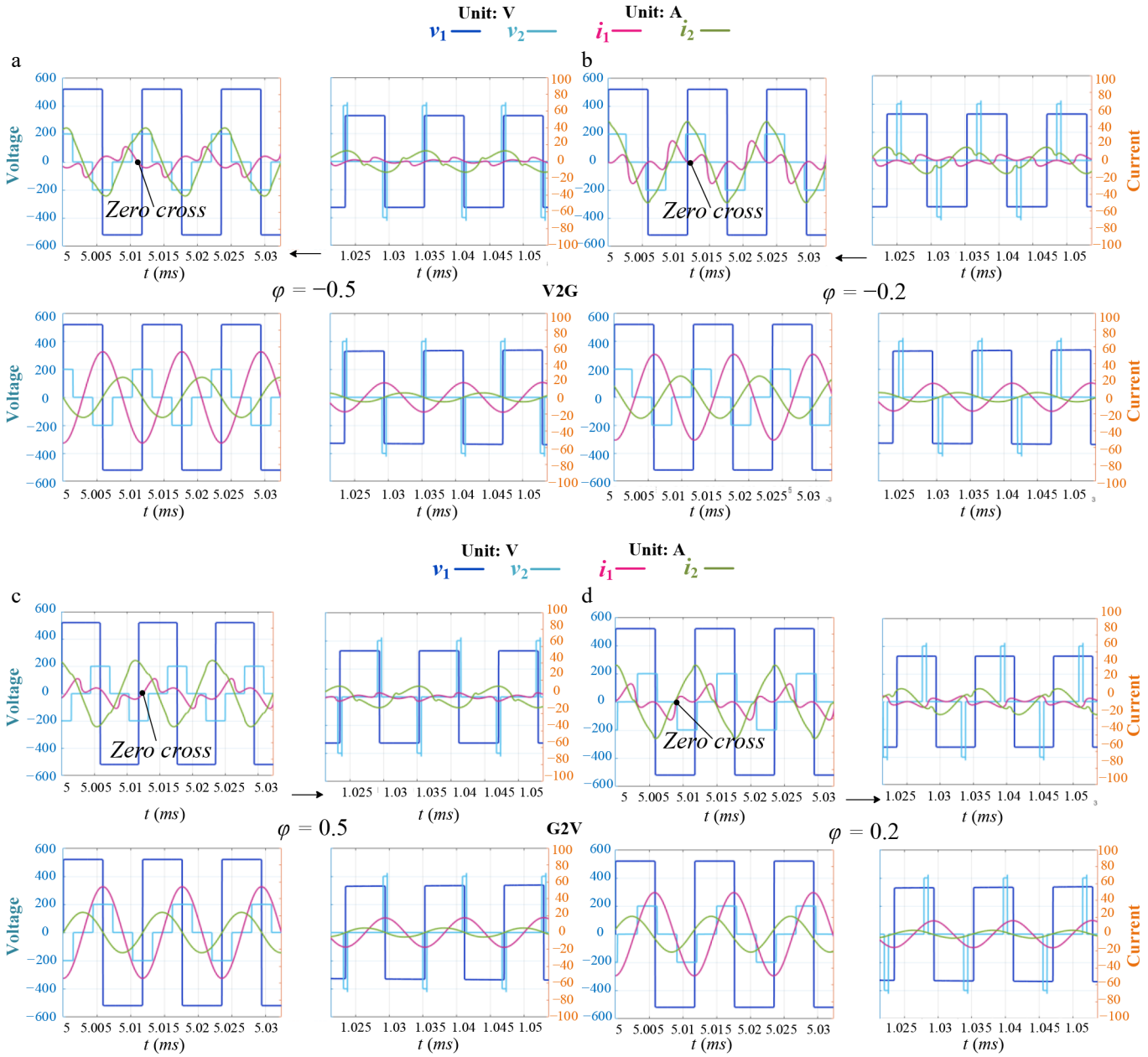

Fig. 9 Theory derivation of voltage and current in steady state (left: max v_{ac}; right: low v_{ac}). (a) $\varphi = -0.5$ for V2G. (b) $\varphi = -0.2$ for V2G. (c) $\varphi = 0.5$ for G2V. (d) $\varphi = 0.2$ for G2V.

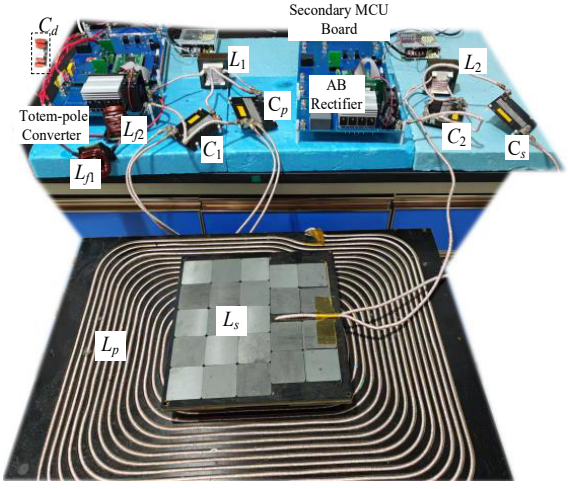

Fig. 10 BWPT system experiment test bench.

error for i_1 is relatively larger. This is mainly due to a phase shift between the peak value and the actual comparison. Nevertheless, the error remains within 20%, and the zero-crossing errors for both i_1 and i_2 can be kept within 5%. Therefore, based on these theoretical results, the soft-switching status of the switch tubes can be accurately determined.

The results above can also be validated by Fig. 17, which demonstrates that the results from the FTDC theory closely reflect the experimental outcomes, thus effectively achieving the goal of waveform prediction.

Tables 3 and 4 present detailed data of FTDC calculation and experiment from Figs 16 and 17 with $\varphi = +0.5$ and $\varphi = -0.1$.

Table 5 presents a comparison of different WPT modeling methods. FHA, Generalized Space-State Averaging (GSSA), TMH, and sample-data model[11] all focus on obtaining the average state of the system, with ample-data model being applicable only to Series-Series (SS) topologies and unidirectional energy transfer

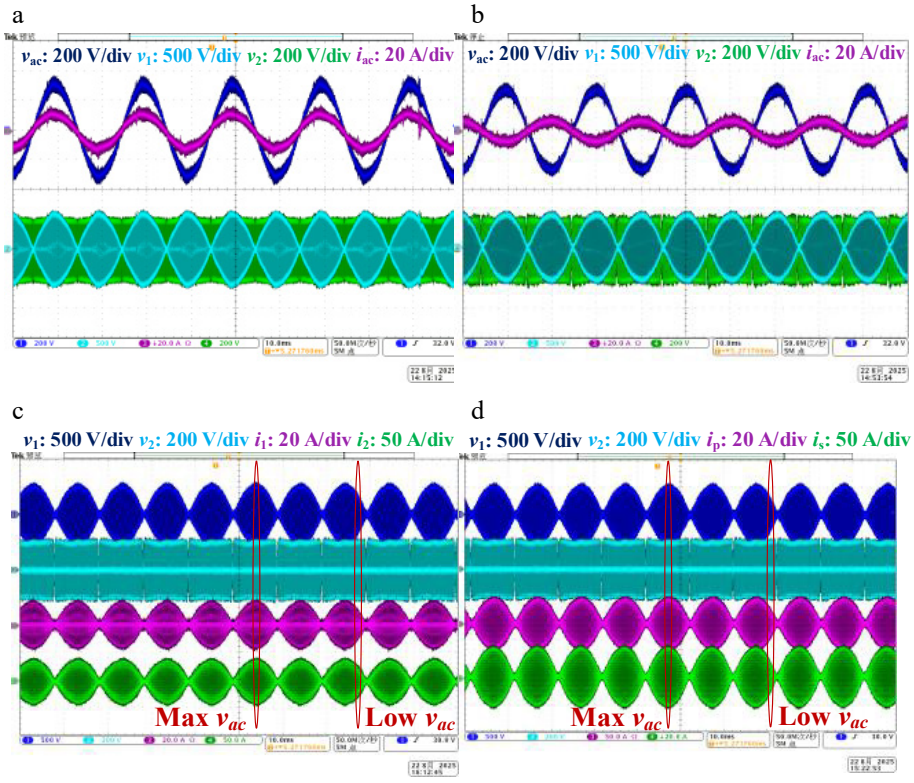

Fig. 11 Specific experiment waveforms of BWPT system. (a) $\varphi = 0.5$ for G2V. (b) $\varphi = -0.3$ for V2G. (c) Steady-state waveforms with i_1 and i_2. (d) Steady-state waveforms with i_p and i_s.

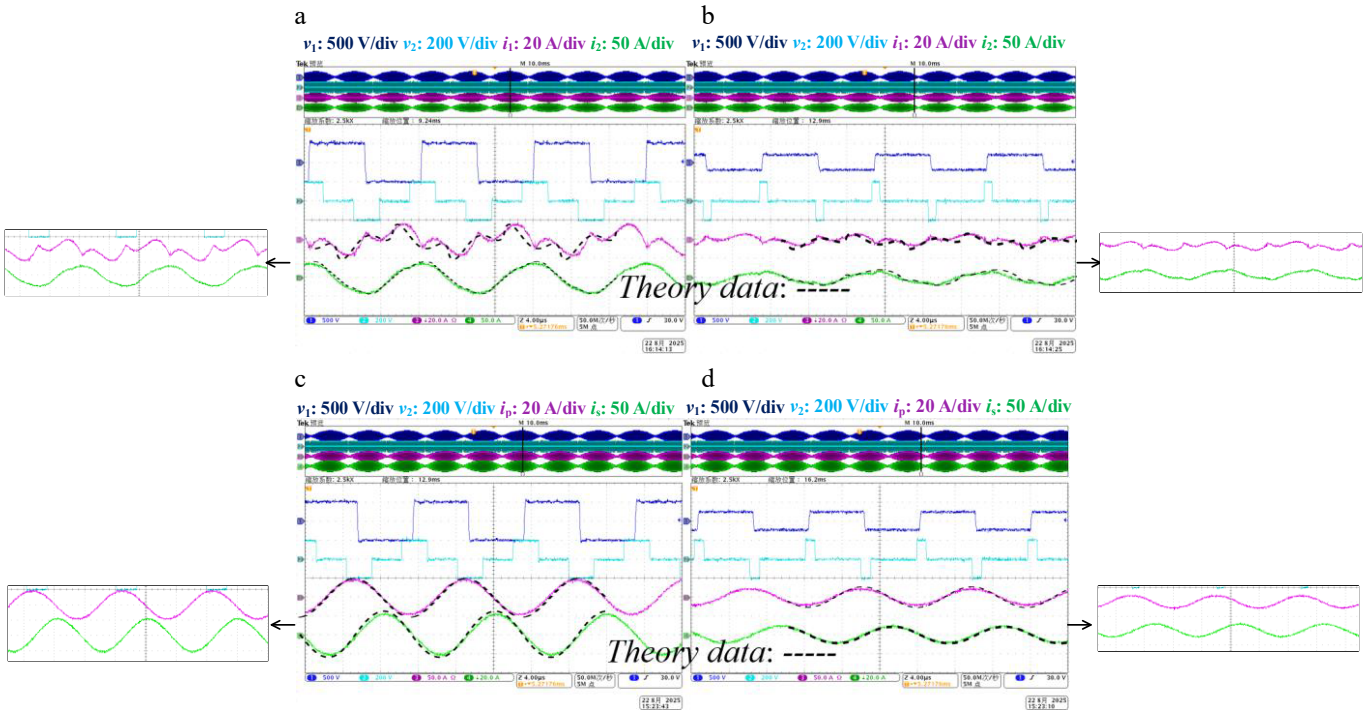

Fig. 12 Experiment validation of $\varphi = -0.5$ for V2G. (a) Maximum v_{ac} with i_1 and i_2. (b) Low v_{ac} with i_1 and i_2. (c) Steady-state waveforms with i_p and i_s. (d) Low v_{ac} with i_p and i_s.

applications. Methods of time-domain analysis[12–13] employ complex frequency domain analysis, with discrete-time model[13] specifically designed for DLCC systems but not supporting BWPT systems. The approach outlined in this paper, however, not only models the system characteristics in both G2V and V2G directions but also achieves a lower-order representation, ensuring both a manageable computational load and accurate results.

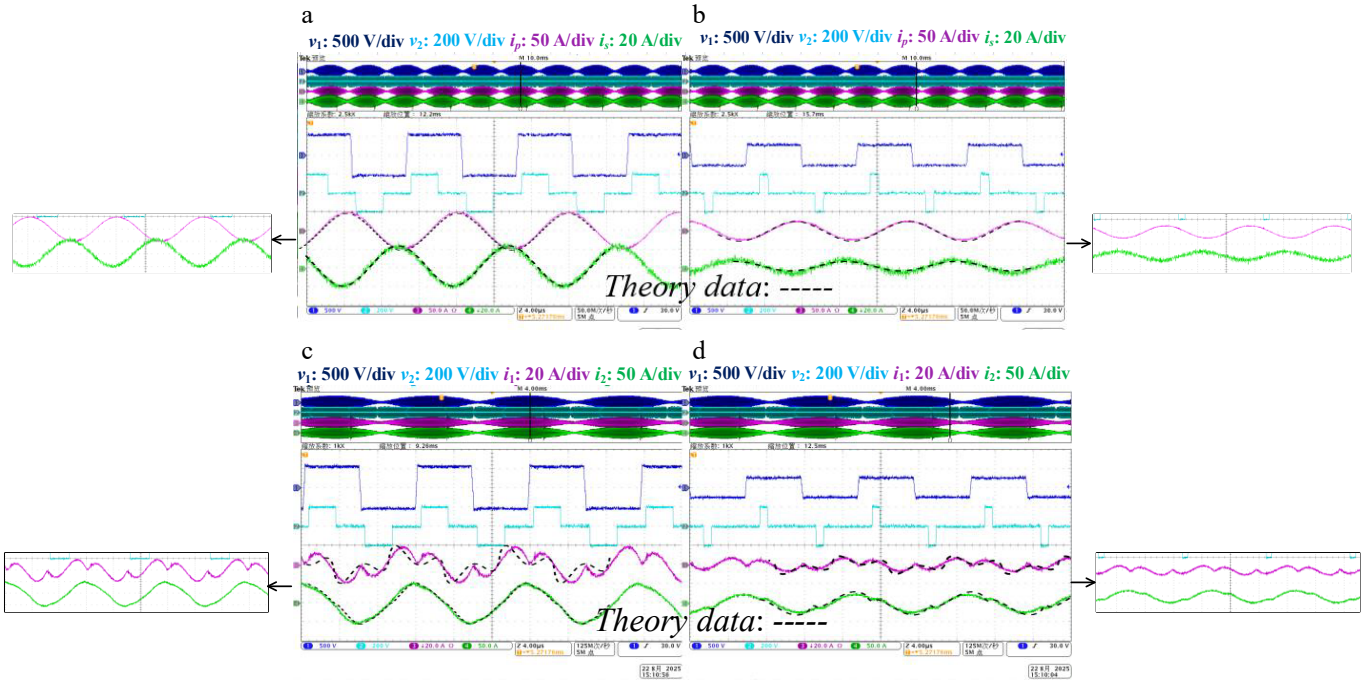

Fig. 13 Experiment validation of $\varphi = -0.2$ for V2G. (a) Maximum v_{ac} with i_1 and i_2. (b) Low v_{ac} with i_1 and i_2. (c) Maximum v_{ac} with i_p and i_s. (d) Low v_{ac} with i_p and i_s

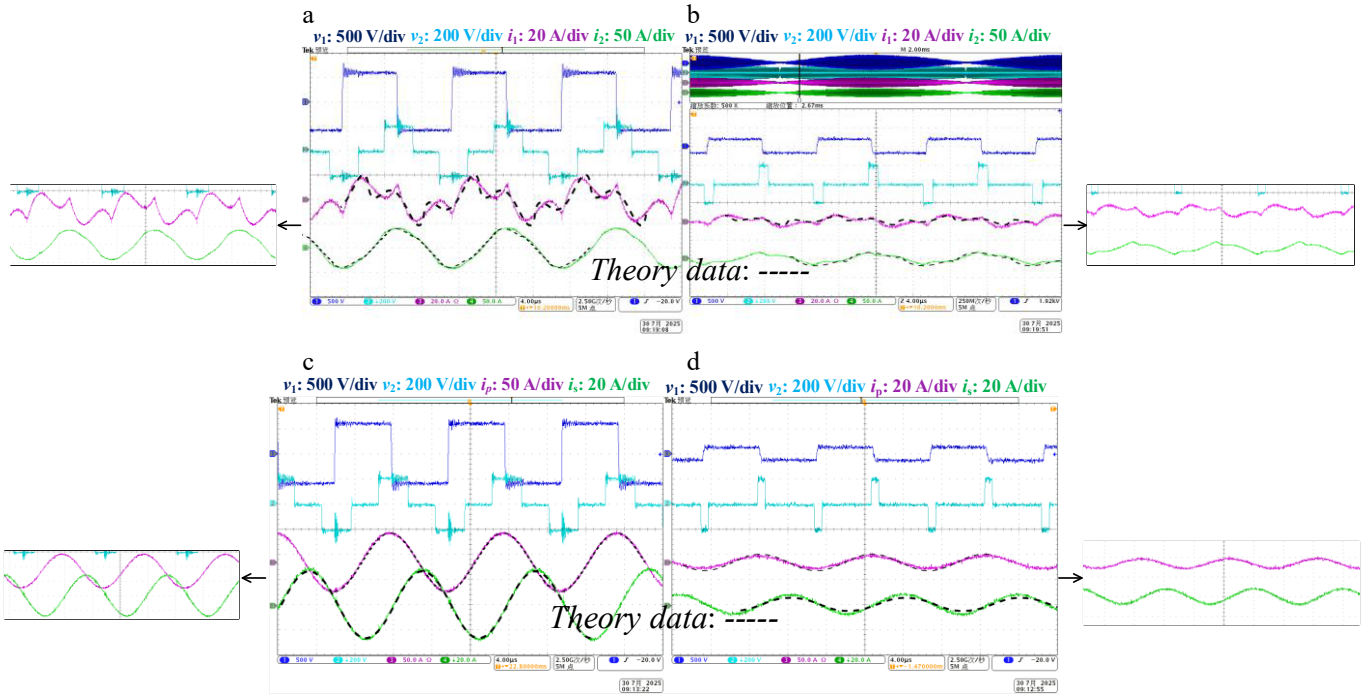

Fig. 14 Experiment validation of $\varphi = 0.5$ for G2V. (a) Maximum v_{ac} with i_1 and i_2. (b) Low v_{ac} with i_1 and i_2. (c) Maximum v_{ac} with i_p and i_s. (d) Low v_{ac} with i_p and i_s.

Conclusions

To address the result deviation caused by primary-secondary phase difference when using the TMH method, this paper presents an FTDC analysis prediction method for the BWPT system using a single-stage totem-pole AC-AC converter. First, it analyzes the harmonics composition of the input and output voltage and current within the passive network, providing expressions for each component of the passive impedance like the TMH method. Then, the harmonics reconstruction based on the phase correction of the voltage and current variables are derived using the homogeneous and superposition theorems. Theoretical expressions and waveforms for voltage and current are then obtained by combining both frequency-domain and time-domain methods. Experimental results are used to validate the consistency between the theoretical and measured waveforms. Additionally, the paper investigates deviations in current amplitude, effective value, phase, and zero-crossing points compared to experimental data, confirming the accuracy of

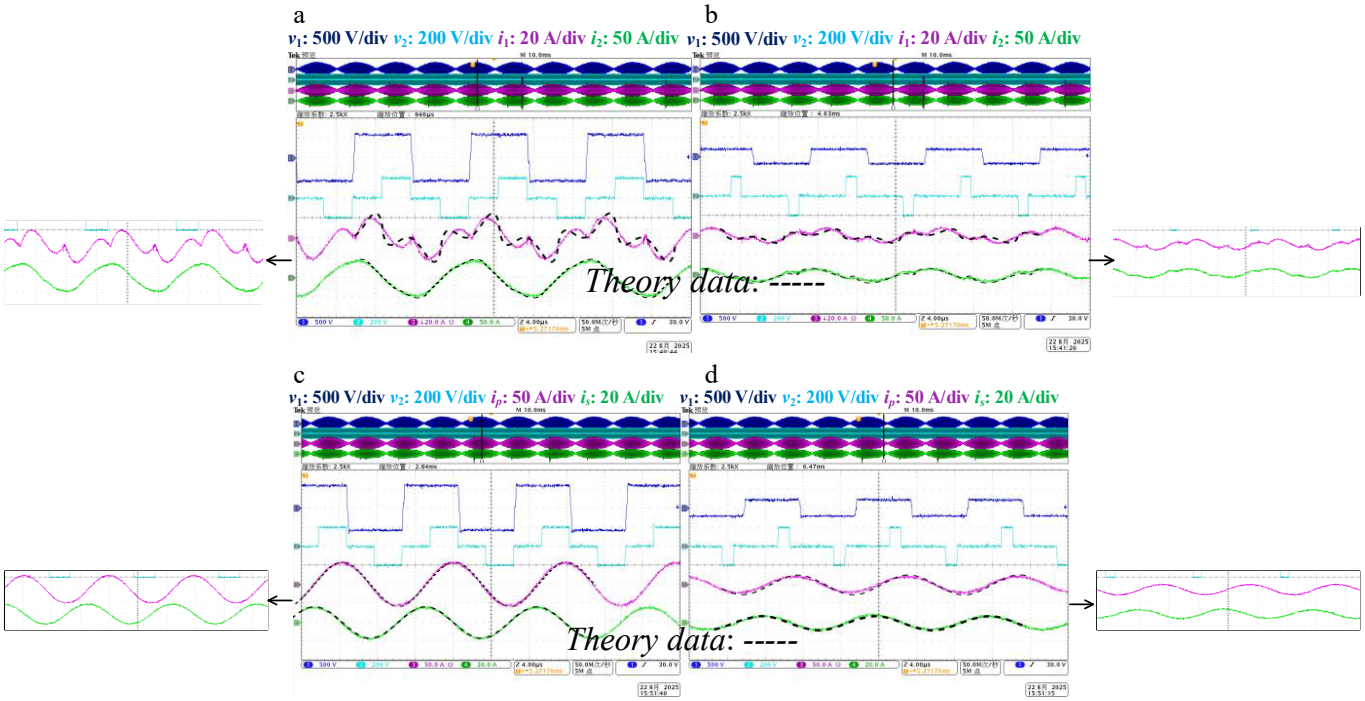

Fig. 15 Experiment validation of $\varphi = 0.2$ for G2V. (a) Maximum v_{ac} with i_1 and i_2. (b) Low v_{ac} with i_1 and i_2. (c) Maximum v_{ac} with i_p and i_s. (d) Low v_{ac} with i_p and i_s.

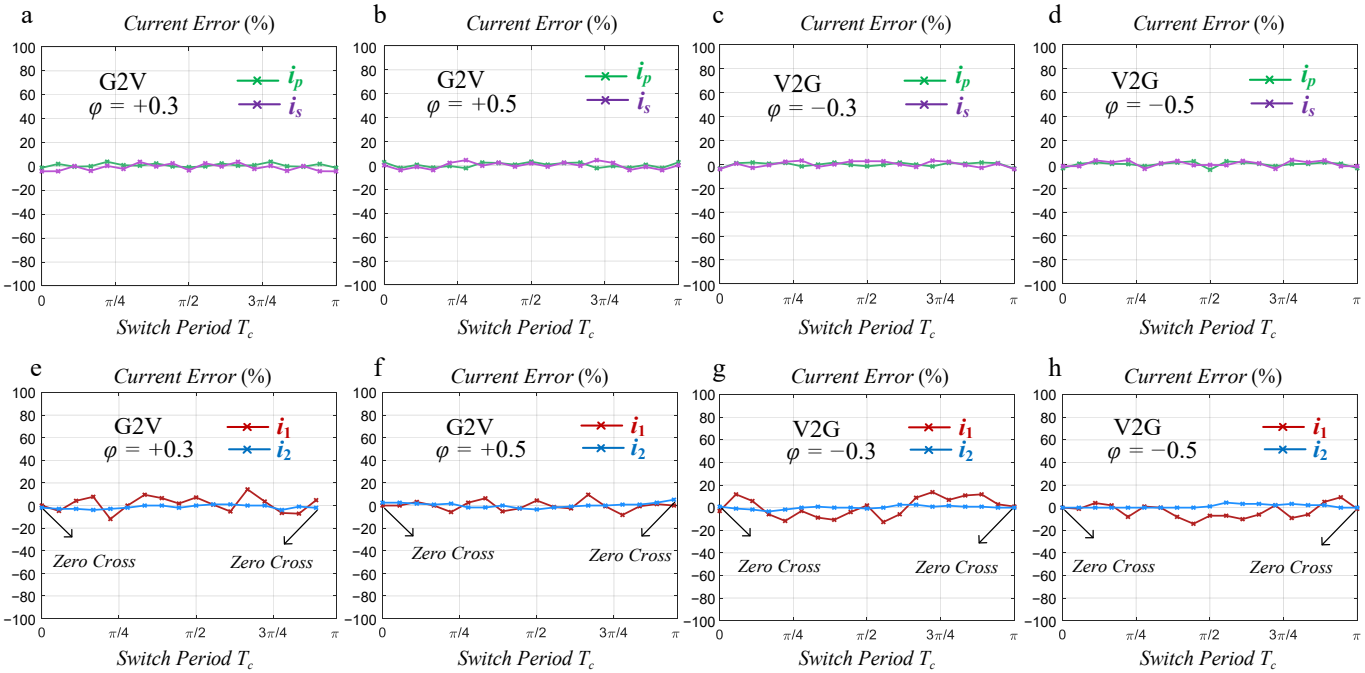

Fig. 16 The error of passive network currents under different phase shifts and different power transfer directions. (a) i_p and i_s for $\varphi = +0.3$. (b) i_p and i_s for $\varphi = +0.5$. (c) i_p and i_s for $\varphi = -0.3$. (d) i_p and i_s for $\varphi = -0.5$. (e) i_1 and i_2 for $\varphi = +0.3$. (f) i_1 and i_2 for $\varphi = +0.5$. (g) i_1 and i_2 for $\varphi = -0.3$. (h) i_1 and i_2 for $\varphi = -0.5$.

the proposed analytical method. Finally, for the complex system of a single-stage AC-AC converter in the BWPT setup, the FTDC analysis method effectively provides accurate theoretical results across various operating points.

Author contributions

The authors confirm contribution to the paper as follows: study conception and design: Zhang X, Zhang Q, Wu H, Dong S; data collection: Zhang X; software: Zhang X; validation: Zhang X, Zhang Q; analysis and interpretation of results: Zhang X, Zhang Q, Wu H, Dong S; draft manuscript preparation: Zhang X, Zhang Q, Wu H, Dong S; supervision: Zhang Q. All authors reviewed the results and approved the final version of the manuscript.

Data availability

All data that support the findings of this study are available upon reasonable request from the corresponding author.

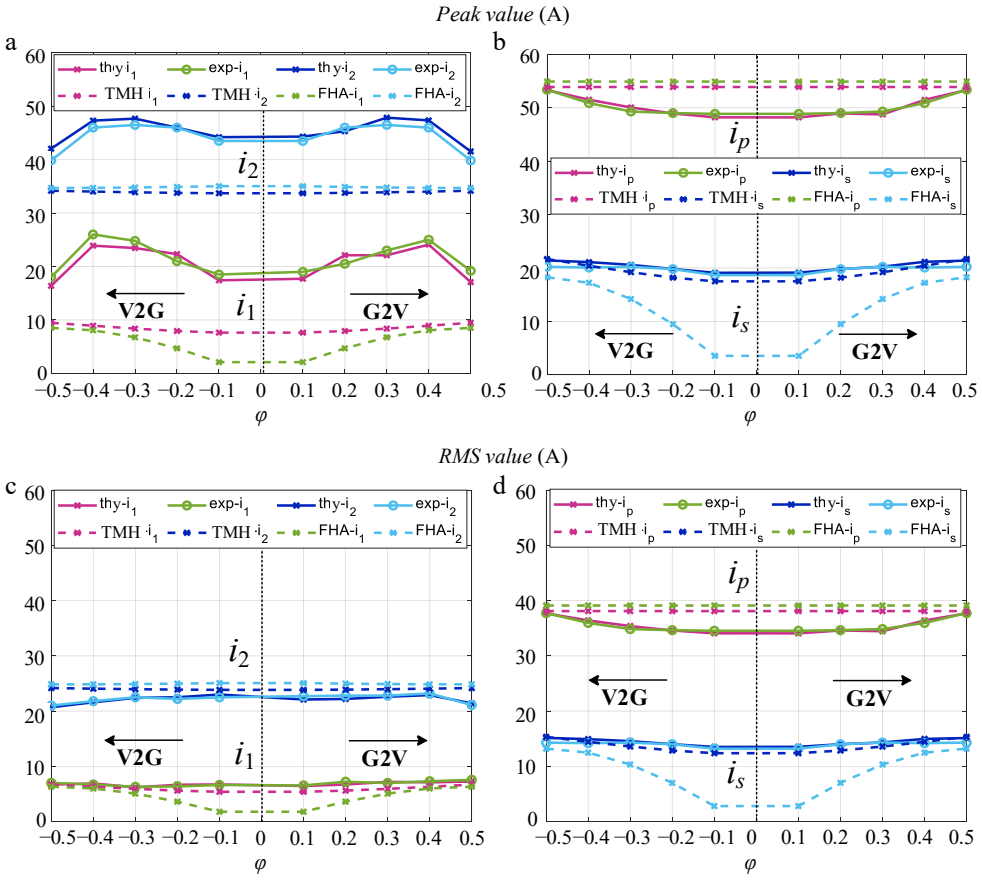

Fig. 17 Experiment validation data ('thy' for 'theory', 'exp' for 'experiment'). (a) i_1 and i_2 for amplitude. (b) i_p and i_s for amplitude. (c) i_1 and i_2 for RMS value. (d) i_p and i_s for RMS value.

Table 3. Detailed data of FTDC calculation and experiment with $\varphi = +0.5$.

Method type	Peak value (A)				RMS value (A)				Mean value of current error			
	i_1	i_2	i_p	i_s	i_1	i_2	i_p	i_s	i_1	i_2	i_p	i_s
FHA	9.1	34.8	55.8	17.6	7.6	25.1	39.8	13.3	/	/	/	/
TMH	9.8	34.4	55.5	20.9	8.2	24.6	38.5	15.6	/	/	/	/
thy(FTDC)	17.7	42.0	55.3	20.9	8.3	20.6	38.4	15.5	7.8%	2.1%	1.2%	1.9%
exp(Experiment)	19.6	39.9	55.3	20.0	8.3	20.6	38.4	14.7				

Table 4. Detailed data of FTDC calculation and experiment with $\varphi = -0.3$.

Method type	Peak value (A)				RMS value (A)				Mean value of current error			
	i_1	i_2	i_p	i_s	i_1	i_2	i_p	i_s	i_1	i_2	i_p	i_s
FHA	4.8	35	55.8	14.2	5.8	24.9	39.8	10.2	/	/	/	/
TMH	9.2	34.7	54.9	19.3	6.2	23.6	37.9	13.6	/	/	/	/
thy(FTDC)	23.3	47.9	50.0	20.3	6.3	22.8	35.5	14.8	12.2%	2.3%	1.7%	1.8%
exp(Experiment)	24.8	46.1	49.7	20.2	6.2	22.8	35.3	14.7				

Table 5. Comparison between various methods in WPT application.

Method type	Amount of calculation	Number of order n	BWPT support	Computational complexity	Compensation network	Three feature outputs	Accuracy (for feature outputs)
FHA	Small	1	Yes	Simple	Unrestricted	Average only	Low
GSSA	Large	Infinite	Yes	Very complex	Unrestricted	Average only	High
TMH analysis[18–20]	Medium	Not mentioned	No	Medium	Unrestricted	All	Medium
Sample-data model[21]	Large	Infinite	No	Complex	SS	Average only	Very high
harmonics-considered time-domain model[22]	Small	Not mentioned	No	Medium	Unrestricted	All	Medium
Discrete-time model[23]	Very large	9	No	Complex	DLCC	All	Very high
Proposed FTDC	Medium	3, 9	Yes	Medium	Unrestricted	All	High

Conflict of interest

The authors declare that they have no conflict of interest.

Dates

Received 31 July 2025; Revised 8 September 2025; Accepted 8 October 2025; Published online 25 December 2025

References

1. Wang L, Madawala UK, Wong MC. 2021. A wireless vehicle-to-grid-to-home power interface with an adaptive DC link. *IEEE Journal of Emerging and Selected Topics in Power Electronics* 9:2373–83
2. Liu Y, Jin D, Jiang S, Liang W, Peng J, et al. 2019. An active damping control method for the LLCL filter-based SiC MOSFET grid-connected inverter in vehicle-to-grid application. *IEEE Transactions on Vehicular Technology* 68:3411–23
3. Verma A, Singh B. 2021. AFF-SOGI-DRC control of renewable energy based grid interactive charging station for EV with power quality improvement. *IEEE Transactions on Industry Applications* 57:588–97
4. Liu H, Hu Z, Song Y, Lin J. 2013. Decentralized vehicle-to-grid control for primary frequency regulation considering charging demands. *IEEE Transactions on Power Systems* 28:3480–89
5. Zhang Y, Guan S, Zhang Y. 2019. Single-stage AC-AC converter with controllable phase and amplitude. *IEEE Transactions on Power Electronics* 34:6991–7000
6. Weerasinghe S, Madawala UK, Thrimawithana DJ. 2017. A matrix converter-based bidirectional contactless grid interface. *IEEE Transactions on Power Electronics* 32:1755–66
7. Samanta S, Rathore AK. 2018. A new inductive power transfer topology using direct AC-AC converter with active source current waveshaping. *IEEE Transactions on Power Electronics* 33:5565–77
8. Kumar J, Samanta S. 2024. A single-stage universal input wireless inductive power transfer system with V2G capability. *IEEE Journal of Emerging and Selected Topics in Industrial Electronics* 5:1017–29
9. Khan AA, Cha H, Ahmed HF. 2016. High-efficiency single-phase AC-AC converters without commutation problem. *IEEE Transactions on Power Electronics* 31:5655–65
10. Tan PA, Lei W, Wang B, Xu X. 2024. A dual-output AC-AC converter for double transmitter wireless power transfer systems. *IEEE Transactions on Industrial Electronics* 71:12131–40
11. Khan AA, Cha H, Kim HG. 2016. Magnetic integration of discrete-coupled inductors in single-phase direct PWM AC-AC converters. *IEEE Transactions on Power Electronics* 31:2129–38
12. Shin HH, Cha H, Kim HG, Yoo DW. 2015. Novel single-phase PWM AC-AC converters solving commutation problem using switching cell structure and coupled inductor. *IEEE Transactions on Power Electronics* 30:2137–47
13. Mishima T, Sakamoto S, Ide C. 2017. ZVS phase-shift PWM-controlled single-stage boost full-bridge AC-AC converter for high-frequency induction heating applications. *IEEE Transactions on Industrial Electronics* 64:2054–61
14. Belkamel H, Kim H, Choi S. 2021. Interleaved totem-pole ZVS converter operating in CCM for single-stage bidirectional AC-DC conversion with high-frequency isolation. *IEEE Transactions on Power Electronics* 36:3486–95
15. Zhang X, Zhang Q, Zhang F. 2025. Triple phase ratio shift control for bidirectional wireless power transfer application based on totem-pole single-stage AC-AC converter. *IEEE Transactions on Power Electronics* 40:11863–73
16. Swain AK, Neath MJ, Madawala UK, Thrimawithana DJ. 2012. A dynamic multivariable state-space model for bidirectional inductive power transfer systems. *IEEE Transactions on Power Electronics* 27:4772–80
17. Mohamed AAS, Berzoy A, Mohammed OA. 2017. Experimental validation of comprehensive steady-state analytical model of bidirectional WPT system in EVs applications. *IEEE Transactions on Vehicular Technology* 66:5584–94
18. Hu J, Zhao J, Cui C. 2021. A wide charging range wireless power transfer control system with harmonic current to estimate the coupling coefficient. *IEEE Transactions on Power Electronics* 36:5082–94
19. Hu J, Zhao J, Gao F. 2023. A real-time maximum efficiency tracking for wireless power transfer systems based on harmonic-informatization. *IEEE Transactions on Power Electronics* 38:1275–87
20. Liu W, Chau KT, Lee CHT, Tian X, Jiang C. 2021. Hybrid frequency pacing for high-order transformed wireless power transfer. *IEEE Transactions on Power Electronics* 36:1157–70
21. Tang J, Dong S, Cui C, Zhang Q. 2020. Sampled-data modeling for wireless power transfer systems. *IEEE Transactions on Power Electronics* 35:3173–82
22. Fu N, Deng J, Wang Z, Wang W, Wang S. 2022. A hybrid mode control strategy for LCC-LCC-compensated WPT system with wide ZVS operation. *IEEE Transactions on Power Electronics* 37:2449–60
23. He K, Liu X, Gao F, Yang X, Cheng Z, et al. 2024. Accurate discrete-time modeling and boundary analysis for high-order wireless power transfer systems. *IEEE Transactions on Power Electronics* 39:16839–54
24. Liu J, Xu F, Sun C, Loo KH. 2023. A compact single-phase AC-DC wireless power transfer converter with active power factor correction. *IEEE Transactions on Industrial Electronics* 70:3685–96
25. Mohamed AAS, Mohammed O. 2019. Bilayer predictive power flow controller for bidirectional operation of wirelessly connected electric vehicles. *IEEE Transactions on Industry Applications* 55:4258–67